

A locally DIV-free projection scheme for incompressible flows based on non-conforming finite elements

B. Bejanov^{1,‡}, J.-L. Guermond^{2,3,§} and P. D. Minev^{1,*,†}

¹*Department of Mathematical and Statistical Sciences, University of Alberta, Edmonton, Canada T6G 2G1*

²*Department of Mathematics, Texas A&M University 3368 TAMU, College Station, TX 77843-3368, U.S.A.*

³*LIMSI-CNRS UPR 3251, BP 133, Orsay, France*

SUMMARY

We present a projection scheme whose end-of-step velocity is locally pointwise divergence free, using a continuous \mathbb{P}_1 approximation for the velocity in the momentum equation, a first-order Crouzeix–Raviart approximation at the projection step, and a \mathbb{P}_0 approximation for the pressure in both steps. The analysis of the scheme is done only for grids that guarantee the existence of a divergence free conforming \mathbb{P}_1 interpolant for the velocity. Optimal estimates for the velocity error in L^2 - and H^1 -norms are deduced. The numerical results demonstrate that these estimates should also hold on grids on which the continuous \mathbb{P}_1 approximation for the velocity locks. Since the end-of-step velocity is locally solenoidal, the scheme is recommendable for problems requiring good mass conservation. Copyright © 2005 John Wiley & Sons, Ltd.

KEY WORDS: projection schemes; divergence-free elements; incompressible Navier–Stokes equations

1. INTRODUCTION

The numerical solution of the incompressible Navier–Stokes equations has been the focus of the CFD community for over five decades. Yet, the quest for an optimal scheme, in terms of cost and accuracy, is not over. It is quite clear now that the solution (via Uzawa iterations) of the coupled velocity–pressure discrete system that results from the space and time discretization of the equations is quite expensive. Moreover, in most situations, the exact

*Correspondence to: P. D. Minev, Department of Mathematical and Statistical Sciences, University of Alberta, Edmonton, Canada T6G 2G1.

†E-mail: minev@ualberta.ca

‡E-mail: bbejanov@math.ualberta.ca

§E-mail: guermond@math.tamu.edu

Contract/grant sponsor: National Science and Engineering Research Council of Canada

Received 21 July 2004

Revised 19 April 2005

Accepted 24 April 2005

Copyright © 2005 John Wiley & Sons, Ltd.

(better to say highly accurate) solution of this system is not necessary. Rather than that, it is often enough to find some easy-to-compute approximation to this solution because it is itself an approximation of some order to the solution of the continuous equations. By far, the most popular way to build such approximations is the so-called projection approach. The method rests on the well known decomposition of L^2 -vector fields into the direct sum of divergence-free fields and curl-free fields (see Reference [1] for details). From the linear algebra point of view, the method relies on the fact that, if both the momentum equation and the Schur complement for the pressure are well enough preconditioned, one Uzawa iteration for the coupled system yields an approximate velocity which has the same order of accuracy as that of the coupled system. The solution for the pressure, however, may be less accurate (depending on the initial guess). Starting with the pioneering works of Temam [2] and Chorin [3] the development of projection schemes continued for over thirty years. For a recent review and error analysis of the most popular of these schemes the reader is referred to References [4–6] and the many references therein. These algorithms can also be considered as splitting schemes in time, and the splitting accuracy so far seems to be limited to second-order in time. The most accurate second-order schemes available are the so-called incremental pressure-correction and velocity-correction schemes in rotational form (see References [4, 5]). The various approximate factorization schemes (see for example Reference [7]) which split the discrete coupled system rather than the system of PDEs can be shown to be equivalent to some of the continuous approaches (see Reference [6]).

Many of the available projection methods use a continuous approximation for the pressure which allows the projection step to take the form of a Poisson equation (see References [8, 9]). Although the choice for the pressure approximation is not limited to continuous approximations only, there are not many studies involving discontinuous pressure approximations and a mixed form of the Poisson equation for the pressure. The main advantage of such elements is that they are locally (elementwise) conservative. Gresho and Sani [10] discuss a projection with \mathbb{Q}_1 – \mathbb{Q}_0 elements which are generally unstable for the pressure but, using proper grids, yield impressive results. Rannacher and Turek [11] suggested the inf–sup stable rotated multilinear element which involves velocities spanned by $(x^2 - y^2, x, y, 1)$ and a piecewise constant pressure over quadrilateral elements (in two dimensions). An advantage of this element is that it leads to linear systems which can be efficiently solved with multigrid methods. Another non-conforming first-order element which is inf–sup stable and locally conservative is the triangular element suggested by Crouzeix and Raviart (see Reference [12]). It has not been very popular among practitioners mainly because it yields a significantly larger linear system for the velocity compared to the continuous piecewise linear \mathbb{P}_1 approximation. It involves two unknowns for the velocity on each internal edge of the grid in two dimensions. This is usually a much larger number compared to the number of unknowns for a \mathbb{P}_1 approximation which involves two unknowns per internal node. If n_k is the number of elements in a triangular grid, n_e the number of internal edges, and n_v the number of internal vertices, the Euler–Poincaré’s formula (in two dimensions) gives $n_e = n_k + n_v - 1$. On two-dimensional grids constructed by division of quadrilaterals, it is possible to condense the unknowns corresponding to the diagonal that subdivides each quadrilateral so as to obtain a linear system of the same size as the one which is based on nodal basis functions. However, in three dimensions this condensation is quite technical, and the linear system following from the momentum equation is significantly larger than the one based on nodal basis functions. The most significant advantage of this non-conforming approximation is that the divergence of the velocity field is zero inside each

element (note that this is not the case with the Rannacher–Turek element because its basis contains second-order terms).

The present study is an attempt to compromise between the inf–sup stable and locally conservative first-order Crouzeix–Raviart element $\mathbb{P}_1^{\text{nc}}-\mathbb{P}_0$ and the computationally efficient $\mathbb{P}_1-\mathbb{P}_0$ element. The second element is known to lock on some grids and therefore is not suitable for unstructured grids. In this study, we propose to solve the momentum equation using a continuous piecewise linear approximation for the velocity, and then to project it onto the Crouzeix–Raviart space composed of the functions that are locally solenoidal using an L_2 -projection. Although it is not yet fully established that methods that locally enforce mass conservation are advantageous compared to those that do not, it seems that this property is desirable in advection-dominated problems (see Reference [13]) and is also a desirable feature when the computed velocity field is used for the transport of scalar fields (free-boundary problems, heat convection, etc). If in these problems the velocity is not solenoidal, the advection equation for the scalar cannot be written in a conservative form which results in a loss of mass that can be significant if the integration time is long enough.

The remainder of the paper is organized as follows. In Section 2 we present the projection method, the implementation of the projection step, and we discuss the accuracy of the method. In Section 3, we present extensive numerical data demonstrating the accuracy of the method.

2. DESCRIPTION AND ANALYSIS OF THE SCHEME

2.1. Preliminary results

Let us consider the Dirichlet initial-boundary value problem for the Navier–Stokes equations

$$\begin{aligned} \frac{\partial \mathbf{u}}{\partial t} + (\mathbf{u} \cdot \nabla)\mathbf{u} &= -\nabla p + \frac{1}{Re} \nabla^2 \mathbf{u} + \mathbf{f} \quad \text{in } \Omega \times (0, T) \\ \nabla \cdot \mathbf{u} &= 0 \quad \text{in } \Omega \times (0, T) \\ \mathbf{u} &= 0 \quad \text{on } \partial\Omega \times (0, T), \quad \mathbf{u} = \mathbf{u}_0 \quad \text{on } \Omega \times \{0\} \end{aligned} \tag{1}$$

where Ω is a smooth, open, bounded, and connected domain in \mathbb{R}^d , ($d=2, 3$). We assume that Ω is such that the H^2 -regularity property holds for the steady Stokes problem in Ω . As it will be clear later, the technique proposed in this paper can be generalized to three dimensions but for the sake of clarity and simplicity all the considerations are confined to the two-dimensional case.

Let \mathcal{T}_h be a regular triangulation of Ω using affine triangles of size h , and consider the following piecewise polynomial spaces:

$$\mathbf{X}_h = \{ \mathbf{v}_h \in \mathbf{H}_0^1(\Omega); \mathbf{v}_{h|e} \in (\mathbb{P}_1(e))^d \quad \forall e \in \mathcal{T}_h \}$$

where $\mathbb{P}_1(e)$ is the space of all affine functions on the element e . In addition, we will need the so-called Crouzeix–Raviart piecewise polynomial spaces which are defined as follows. Upon denoting by $m_{i,e}$ the midpoint of the i th side of the e th element ($i=1, 2, 3$), we set

$$\begin{aligned} \mathbf{Y}_h &= \{ \mathbf{v}_h \in \mathbf{L}^2(\Omega); \mathbf{v}_h \in (\mathbb{P}_1(e))^d \quad \forall e \in \mathcal{T}_h; \mathbf{v}_h \text{ is continuous at } m_{i,e} \in \Omega \\ &\quad \mathbf{v}_h(m_{j,h}) = 0 \quad \forall m_{j,h} \in \partial\Omega \} \end{aligned}$$

$$\mathbf{V}_h = \{\mathbf{v}_h \in \mathbf{Y}_h; \nabla \cdot \mathbf{v}_h|_e = 0 \quad \forall e \in \mathcal{T}_h\}$$

$$\mathcal{Q}_h = \left\{ q_h \in L^2(\Omega); q_h|_e = \mathbb{P}_0(e) \quad \forall e \in \mathcal{T}_h; \int_{\Omega} q_h = 0 \right\}$$

We now assume that there exists a subspace $\hat{\mathcal{Q}}_h \subset \mathcal{Q}_h$ such that the couple $(\mathbf{X}_h, \hat{\mathcal{Q}}_h)$ satisfies a uniform inf-sup condition and $\hat{\mathcal{Q}}_h$ has optimal interpolation properties. Moreover, we assume that $\hat{\mathcal{Q}}_h$ has an orthogonal complement $\tilde{\mathcal{Q}}_h$ such that $(\nabla \cdot \mathbf{v}_h, \tilde{q}_h) = 0$ for all \tilde{q}_h in $\tilde{\mathcal{Q}}_h$ and all \mathbf{v}_h in \mathbf{X}_h . Such spaces are known to exist if \mathcal{T}_h is a so-called cross-grid, see, e.g. Reference [14].

Let us consider the following interpolation problem:

$$\begin{aligned} &\text{Find } \mathbf{w}_h(t) \in \mathbf{X}_h \text{ and } \hat{q}_h(t) \in \hat{\mathcal{Q}}_h \text{ such that } \forall \mathbf{v}_h \in \mathbf{X}_h, \forall r_x \in \mathcal{Q}_h \\ &(\nabla \mathbf{w}_h(t), \nabla \mathbf{v}_h)_\Omega - (\hat{q}_h(t), \nabla \cdot \mathbf{v}_h)_\Omega = (\nabla \mathbf{u}(t), \nabla \mathbf{v}_h)_\Omega - (p(t), \nabla \cdot \mathbf{v}_h)_\Omega \\ &(\nabla \cdot \mathbf{w}_h(t), r_x)_\Omega = (\nabla \cdot \mathbf{u}(t), r_x)_\Omega \end{aligned} \quad (2)$$

where $\mathbf{u}(t)$, $p(t)$ is the solution of (1). Here and in the remainder of the paper $(v, w)_E$ denotes the L^2 -inner product of v and w over the domain E (whether E is a measurable manifold of dimension $d - 1$ or a measurable subset of Ω). The L^2 and H^k norms over E are denoted by $\|\cdot\|_{L^2(E)}$ and $\|\cdot\|_{H^k(E)}$ correspondingly.

Lemma 2.1

Provided \mathcal{T}_h is a cross-grid, $\mathbf{u}(t) \in H^2(\Omega)$, $p(t) \in H^1(\Omega)$, $0 \leq t \leq T$, there exists $c > 0$ such that

$$\begin{aligned} &\|\mathbf{u}(t) - \mathbf{w}_h(t)\|_{L^2(\Omega)} + h\|\mathbf{u}(t) - \mathbf{w}_h(t)\|_{\mathbf{H}^1(\Omega)} + h\|p(t) - \hat{q}_h(t)\|_{L^2(\Omega)} \\ &\leq ch^2(\|\mathbf{u}(t)\|_{\mathbf{H}^2(\Omega)} + \|p(t)\|_{L^2(\Omega)}) \end{aligned} \quad (3)$$

This result extends to the time derivatives of the interpolants \mathbf{w}_h , \hat{q}_h if \mathbf{u} and p are smooth enough in time. Note that the interpolant for the velocity is pointwise divergence free. The existence of such a piecewise linear interpolant has been established so far only in the case of cross-grids and its existence is vital for the convergence proof of the method. On the other hand, it is well known that on some grids the \mathbb{P}_1 - \mathbb{P}_0 element locks, i.e. the only piecewise linear divergence free field is $\mathbf{u}_h = 0$. An example of such a grid is the so-called diagonal grid which is produced by first subdividing the domain into quadrilaterals and then subdividing each quadrilateral into two triangles using the equally sloped diagonals (for rectangular domains). The numerical results on such grids (reported in Section 3.1.2) show that the present method is optimally convergent for the velocity.

2.2. Locally divergence free projection

There is a variety of ways to discretize the nonlinear terms. Since we prefer to keep the matrices of the discrete systems symmetric and positive definite, and we want to avoid solving nonlinear discrete systems, and the discretization of the advection is not the focus of this study, we discretize the advection terms by means of a fully explicit (Euler Forward)

scheme. In order to avoid unnecessary complications, since the nonlinear terms do not contribute essentially to the splitting error of projection schemes, we do not take into account the nonlinear terms in the analysis of the method. If we restrict our attention to a first-order scheme, the time splitting and the spatial discretization of (1) proceed as follows: Supposing that proper approximations for the initial velocity and pressure gradient are given by $\mathbf{u}_h^0 \in \mathbf{X}_h$, $\mathbf{G}_h^0 \in \mathbf{Y}_h$ (for the assumptions on these approximations see Section 5.2 of Reference [15]) we solve the following set of problems for $0 \leq n \leq T/\delta t = N$:

- Advection–diffusion step:

Find $\tilde{\mathbf{u}}_h^{n+1} \in \mathbf{X}_h$ such that

$$\begin{aligned} \frac{1}{\delta t} (\tilde{\mathbf{u}}_h^{n+1} - \mathbf{u}_h^n, \tilde{\mathbf{v}}_h)_\Omega + \frac{1}{Re} (\nabla \tilde{\mathbf{u}}_h^{n+1}, \nabla \tilde{\mathbf{v}}_h)_\Omega \\ = \sum_{e \in \mathcal{T}_h} ((\mathbf{u}_h^n \cdot \nabla) \mathbf{u}_h^n, \tilde{\mathbf{v}}_h)_e - (\tilde{\mathbf{v}}_h, \mathbf{G}_h^n)_\Omega + (\mathbf{f}, \tilde{\mathbf{v}}_h)_\Omega \quad \forall \tilde{\mathbf{v}}_h \in \mathbf{X}_h \end{aligned} \tag{4}$$

- Projection step:

Find $\mathbf{u}_h^{n+1} \in \mathbf{V}_h$ such that

$$(\mathbf{u}_h^{n+1} - \tilde{\mathbf{u}}_h^{n+1}, \mathbf{v}_h)_\Omega = 0 \quad \forall \mathbf{v}_h \in \mathbf{V}_h \tag{5}$$

After \mathbf{u}_h^{n+1} is constructed, we correct the pressure gradient, $\mathbf{G}_h^{n+1} \in \mathbf{Y}_h$, so that

$$\mathbf{G}_h^{n+1} - \mathbf{G}_h^n = \frac{\tilde{\mathbf{u}}_h^{n+1} - \mathbf{u}_h^{n+1}}{\delta t} \tag{6}$$

\mathbf{G}_h^{n+1} is then substituted into (4) at the next time step and therefore the last term in (6) is computed in weak form only.

The term \mathbf{G}_h^{n+1} is an approximation of the pressure gradient. To see this, recall that there is a unique $\hat{\phi}_h \in \hat{Q}_h$ such that

$$\begin{aligned} (\mathbf{u}_h^{n+1} - \tilde{\mathbf{u}}_h^{n+1}, \mathbf{v}_h)_\Omega - \sum_{e \in \mathcal{T}_h} (\hat{\phi}_h, \nabla \cdot \mathbf{v}_h)_e = 0 \quad \forall \mathbf{v}_h \in \mathbf{Y}_h \\ \sum_{e \in \mathcal{T}_h} (\nabla \cdot \mathbf{u}_h^{n+1}, q_h)_e = 0 \quad \forall q_h \in Q_h \end{aligned} \tag{7}$$

Then, upon setting $\hat{\phi}_h = p_h^{n+1} - p_h^n$, we observe that $\mathbf{G}_h^{n+1} - \mathbf{G}_h^n$ is nothing more than the Riesz representative in \mathbf{Y}_h of the linear form: $\mathbf{Y}_h \ni \mathbf{v}_h \mapsto (p_h^{n+1} - p_h^n, \nabla \cdot \mathbf{v}_h) \in \mathbb{R}$.

Remark 2.1

The new idea in the proposed scheme concerns the solution of the generalized Stokes problem and this is why in the simulations below we used a simple scheme for advection, the Adams–Bashforth scheme. However, it can be combined with a whole variety of explicit or implicit methods for the advection discretization (e.g. the Adams–Bashforth/Moulton methods, the method of characteristics, GaLS-based methods, etc.).

2.3. Analysis of the scheme

Since the nonlinear term does not contribute essentially to the splitting error of the scheme we do the analysis in the case of the generalized Stokes equations, i.e. skipping the advection terms in (1). A somewhat abstract counterpart of the above setting has been analysed in References [8, 15, 16]. We have three spaces \mathbf{X}_h , \mathbf{Y}_h , and \mathcal{Q}_h . Clearly $\mathbf{X}_h \subset \mathbf{Y}_h$. For $e \in \mathcal{T}_h$ set $|e| = \text{meas}(e)$ and denote by 1_e the characteristic function of e . Define the operators

$$B_h : \mathbf{X}_h \ni \mathbf{v}_h \longrightarrow \sum_{e \in \mathcal{T}_h} 1_K \frac{1}{|e|} \int_e \nabla \cdot \mathbf{v}_h \in \mathcal{Q}_h$$

$$C_h : \mathbf{Y}_h \ni \mathbf{v}_h \longrightarrow \sum_{e \in \mathcal{T}_h} 1_K \frac{1}{|e|} \int_e \nabla \cdot \mathbf{v}_h \in \mathcal{Q}_h$$

It is clear that C_h is an extension of B_h , i.e. for all functions \mathbf{v}_h in \mathbf{X}_h , $B_h \mathbf{v}_h = C_h \mathbf{v}_h$. Note that both these operators are such that

$$(B_h \mathbf{v}_h, q_h)_\Omega = (\nabla \cdot \mathbf{v}_h, q_h)_\Omega \quad \forall (\mathbf{v}_h, q_h) \in \mathbf{X}_h \times \mathcal{Q}_h \quad (8)$$

$$(C_h \mathbf{v}_h, q_h)_\Omega = \sum_{e \in \mathcal{T}_h} \int_e q_h \nabla \cdot \mathbf{v}_h \quad \forall (\mathbf{v}_h, q_h) \in \mathbf{Y}_h \times \mathcal{Q}_h \quad (9)$$

The projection step consists of seeking $\mathbf{u}_h \in \mathbf{Y}_h$ and $\phi_h \in \mathcal{Q}_h$ such that

$$(\mathbf{u}_h^{n+1} - \tilde{\mathbf{u}}_h^{n+1}, \mathbf{v}_h)_\Omega - (C_h \mathbf{v}_h, \phi_h^{n+1})_\Omega = 0 \quad \forall \mathbf{v}_h \in \mathbf{Y}_h \quad (10)$$

$$(C_h \mathbf{u}_h, q_h)_\Omega = 0 \quad \forall q_h \in \mathcal{Q}_h \quad (11)$$

The last hypothesis that must be verified is that C_h^T is uniformly continuous with respect to the H^1 -norm (see [16, Proposition 2.1]).

Let

$$\Pi_h : L^1(\Omega) \ni q \longrightarrow \sum_{e \in \mathcal{T}} 1_e \frac{1}{|e|} \int_e q \in \mathcal{Q}_h$$

Lemma 2.2

There is c independent of h such that

$$\forall q \in H^1(\Omega), \quad \|C_h^T \Pi_h q\|_{L^2(\Omega)} \leq c \|q\|_{H^1(\Omega)}$$

Proof

Owing to the definition of C_h the following holds true:

$$\begin{aligned} \|C_h^T \Pi_h q\|_{L^2(\Omega)}^2 &= (C_h^T \Pi_h q, C_h^T \Pi_h q)_\Omega = \sum_{e \in \mathcal{T}_h} \int_e \Pi_h q \nabla \cdot C_h^T \Pi_h q \\ &= \sum_{e \in \mathcal{T}_h} \int_{\partial e} \Pi_h q (C_h^T \Pi_h q) \cdot \mathbf{n} \end{aligned}$$

For each internal face in the mesh, say f , denote by \bar{q}_f the mean value of the restriction of q to f . Denote by \mathcal{F}_h^i the set of the internal faces and let \bar{q} be the function on \mathcal{F}_h^i whose restriction to $f \in \mathcal{F}_h^i$ is \bar{q}_f . Then, using standard scaling arguments together with the mesh

regularity and Deny–Lions lemma, we infer

$$\begin{aligned} \|C_h^T \Pi_h q\|_{L^2(\Omega)}^2 &= \sum_{e \in \mathcal{T}_h} \int_{\partial e} (\Pi_h q - \bar{q})(C_h^T \Pi_h q) \cdot \mathbf{n} \leq \sum_{e \in \mathcal{T}_h} \|\Pi_h q - \bar{q}\|_{L^2(\partial e)} \|C_h^T \Pi_h q\|_{L^2(\partial e)} \\ &\leq \sum_{e \in \mathcal{T}_h} c h_e^{1/2} \|q\|_{H^1(e)} h_e^{-1/2} \|C_h^T \Pi_h q\|_{L^2(e)} \\ &\leq c \|q\|_{H^1(\Omega)} \|C_h^T \Pi_h q\|_{L^2(\Omega)} \end{aligned}$$

The conclusion follows readily. □

We suppose that the time marching algorithm (4)–(6) is properly initialized (see [15, Section 5.2]) and we denote by $\tilde{\mathbf{e}}^n = \mathbf{u}^n - \tilde{\mathbf{u}}_h^n$ and $\mathbf{e}^n = \mathbf{u}^n - \mathbf{u}_h^n$ the approximation errors of the two steps of the algorithm. Here and further on, we also make use of the notation $r^n = r(t^n)$ whenever r is a time dependent quantity. Let E be a normed space with norm $\|\cdot\|_E$; then for all ϕ in E^N we denote $\|\phi\|_{\ell^2(E)} = (\Delta t \sum_{n=0}^N \|\phi_n\|_E^2)^{1/2}$ and $\|\phi\|_{\ell^\infty(E)} = \max_{n=0}^N \|\phi_n\|_E$.

Theorem 2.1

If the exact solution \mathbf{u}, p satisfies the assumptions of Lemma 2.1 we have

$$\|\tilde{\mathbf{e}}^n\|_{\ell^\infty(L^2(\Omega))} + \|\mathbf{e}^n\|_{\ell^\infty(L^2(\Omega))} \leq c(h^2 + \delta t) \tag{12}$$

$$\|\tilde{\mathbf{e}}^n\|_{\ell^2(H^1(\Omega))} \leq c(h + \delta t) \tag{13}$$

Proof

The proof closely follows the framework established by [8, 15, 16]. □

2.4. L²-projection

The projection step (5) can be performed in several different ways. One possibility is to use the divergence free basis that can be constructed from the linear Crouzeix–Raviart element. This procedure is discussed in detail in References [17, p. 295]. It can be generalized to three dimensions as suggested by Hecht [18]. This basis contains in each triangular element the three tangential components of the Crouzeix–Raviart basis functions and three functions which are linear combinations of the three normal components of the Crouzeix–Raviart basis functions (they correspond to the stream function in two dimensions). The set of tangential basis functions is L^2 -orthogonal to the basis for the stream function. Since they are also mutually orthogonal, the projection step results in a Crouzeix–Raviart field \mathbf{u}^{n+1} whose tangential component at the midpoints of each edge is simply the average of the tangential components of $\tilde{\mathbf{u}}^{n+1}$ at the two extremities of that edge. The computation of the normal components, however, requires the solution of a linear system of equations whose number of unknowns is equal to the number of internal nodes in the grid. Of course, this basis can be used to directly discretize the momentum equation in the Navier–Stokes system thus eliminating the need of projection methods. Unfortunately, the orthogonality property discussed above does not hold with respect to the H^1 -inner product. Therefore, the system for the velocity that results from the momentum equation is fully coupled, and the number of unknowns is equal

to the number of inner edges plus the number of inner nodes in the grid. It is shown in Reference [19] that the stiffness matrix has a condition number of $O(h^{-4})$. There is also numerical evidence that the mass matrix has a condition number of $O(h^{-2})$. On the other hand, the system that results from the \mathbb{P}_1 discretization of the momentum equation is block diagonal and the size of each block is equal to the number of the internal nodes in the grid. The projection step requires the solution of a system of the same size (in 2D) and a condition number similar to the condition number of a Poisson problem with Dirichlet boundary conditions.

In most projection schemes, the L^2 -projection step (5) is performed by introducing a Lagrange multiplier (a pressure correction) and solving the resulting Poisson equation. Since the pressure approximation is piecewise constant in the present case, this approach would require to solve the pressure Poisson equation in mixed form, namely solving the Darcy problem (7). Note, that in the case of first-order Crouzeix–Raviart elements, the mass matrix arising in the discrete form of the first equation in (7) is diagonal because the quadrature based on the midpoints of the finite element edges is exact for the computation of the entries of the mass matrix. Therefore, the construction of the projection matrix can be done explicitly. An alternative approach widely used with mixed methods for elliptic problems is described in Reference [14, p. 178]. It relaxes the continuity requirement on the velocity approximation on the edges of the elements and projects $\tilde{\mathbf{u}}_h^{n+1}$ locally within each element on the divergence free subspace of the local Crouzeix–Raviart space (using one constant Lagrange multiplier for example). The continuity requirement on the element edges is imposed using additional interface Lagrange multipliers. It can be shown that the local L^2 -projection changes only the normal components of $\tilde{\mathbf{u}}_h^{n+1}$ at the midpoints of the faces because the tangential components of the Crouzeix–Raviart bases are divergence free functions. Thus, this approach uses one constant Lagrange multiplier on each edge between two triangles to enforce the continuity of the normal component of the projected velocity. Of course, all these three approaches produce the same solution for the projected velocity. Our numerical experience in 2D is that the projection on the divergence-free basis is by far the fastest. Compared to the solution of (7) without interface multipliers, it reduces the CPU time for the entire algorithm by a factor of (about) two. The introduction of the interface multipliers seem to somewhat improve its performance (particularly at relatively fine grids) but it is still significantly slower than the L^2 -projection onto the divergence-free basis.

2.5. Pressure recovery

The algorithm (4)–(6) does not yield a proper pressure approximation because the general theory requires the spaces X_h and Q_h be inf–sup stable which is not the case here. The numerical results have confirmed that indeed the Lagrange multiplier $\hat{\phi}_h$ used in the projection step (7) does not give a consistent approximation for the pressure correction. Therefore, the pressure should be recovered in a postprocessing step whenever needed. On cross grids it is possible to recover it from the Lagrange multiplier of the projection step (7) (if it is explicitly computed) using the macroelement filtering procedure suggested in Reference [20, Chapter 7]. Although this procedure is very efficient computationally, it is hard to be generalized for other types of grids and therefore we suggest here an alternative postprocessing. As it will become clear, this technique requires the solution of an additional scalar Poisson equation with a Neumann boundary condition and it is therefore more expensive computationally. However,

it should be taken into account that this is just a postprocessing step and therefore it is not necessary to carry it out on each time step.

Consider the following space:

$$M_h = \left\{ q_h \in \mathbf{H}^1(\Omega); q_{h|e} \in (\mathbb{P}_1(e)) \quad \forall e \in \mathcal{T}_h; \int_{\Omega} q_h \, d\Omega = 0 \right\}$$

Then an optimal approximation to the pressure is given by the solution of the following problem: Seek $p_h^{n+1} \in M_h$ such that

$$\begin{aligned} (\nabla p_h^{n+1}, \nabla q_h)_{\Omega} &= -\frac{1}{\delta t} (\tilde{\mathbf{u}}_h^{n+1} - \tilde{\mathbf{u}}_h^n, \nabla q_h)_{\Omega} \\ &\quad - \frac{1}{Re} \int_{\partial\Omega} (\mathbf{n} \times \nabla \times \tilde{\mathbf{u}}_h^{n+1}) \nabla q_h \, ds + (\mathbf{f}^{n+1}, \nabla q_h)_{\Omega} \quad \forall q_h \in M_h \end{aligned} \tag{14}$$

This equation is nothing more than an approximate form of the momentum equation, where we use $\tilde{\mathbf{u}}_h^{n+1}$ to approximate the exact velocity. The surface integral comes from the integration by parts of $\int_{\Omega} (\nabla \times \nabla \times \mathbf{u}) \nabla q_h \, d\Omega = - \int_{\Omega} \nabla^2 \mathbf{u} \nabla q_h \, d\Omega$ (the last identity follows from the well known Helmholtz identity and the fact that $\nabla \cdot \mathbf{u} = 0$). Again, we omit the nonlinear terms (i.e. consider the generalized Stokes equations) because they do not contribute to the error estimate that is proven below. If necessary, they should be taken into account in the right-hand side of (14).

Before we proceed with the proof of the convergence of the pressure approximation, we recall the following result from Reference [15].

Lemma 2.3

If the projection algorithm is properly initialized (see the hypotheses of Reference [15, Lemma 5.6]) we have the following estimate:

$$\|\tilde{\mathbf{e}}_h^{n+1} - \tilde{\mathbf{e}}_h^n\|_{L^2(\mathbf{H}^1(\Omega)^d)} \leq c \delta t (\delta t + h) \tag{15}$$

The accuracy of the pressure approximation given by (14) is the subject of the following theorem.

Theorem 2.2

If the assumptions of Theorem 2.1 and Lemma 2.3 are satisfied then there is $c > 0$ such that

$$\|p^n - p_h^n\|_{L^2(L^2(\Omega))} \leq c(h + \delta t) \tag{16}$$

Proof

We first multiply the first equation in (1) (with the advection terms neglected) by $\nabla q_h \in M_h$, take into account that $\nabla^2 \mathbf{u} = \nabla \nabla \cdot \mathbf{u} - \nabla \times \nabla \times \mathbf{u} = -\nabla \times \nabla \times \mathbf{u}$, and integrate the second-order term by parts. Subtracting the resulting equation from (14) we get the following error equation for the pressure:

$$\begin{aligned} (\nabla(p^{n+1} - p_h^{n+1}), \nabla q_h)_{\Omega} &= -\frac{1}{\delta t} (\tilde{\mathbf{e}}_h^{n+1} - \tilde{\mathbf{e}}_h^n, \nabla q_h)_{\Omega} - \frac{1}{Re} \int_{\partial\Omega} (\mathbf{n} \times \nabla \times \tilde{\mathbf{e}}_h^{n+1}) \nabla q_h \, ds \\ &\quad + \left(\partial_t \mathbf{u}^{n+1} - \frac{\mathbf{u}^{n+1} - \mathbf{u}^n}{\delta t}, \nabla q_h \right)_{\Omega} \end{aligned} \tag{17}$$

Let \hat{p}^{n+1} be the piecewise linear Lagrange interpolant of p^{n+1} , which clearly satisfies the following estimate:

$$\|\nabla(p^{n+1} - \hat{p}^{n+1})\|_{L^2(\Omega)} \leq ch \tag{18}$$

Then we have the following equation for the approximation error $\varepsilon_h^{n+1} = \hat{p}^{n+1} - p_h^{n+1}$:

$$\begin{aligned} (\nabla \varepsilon_h^{n+1}, \nabla q_h)_\Omega &= -\frac{1}{\delta t} (\tilde{\mathbf{e}}_h^{n+1} - \tilde{\mathbf{e}}_h^n, \nabla q_h)_\Omega - \frac{1}{Re} \int_{\partial\Omega} (\mathbf{n} \times \nabla \times \tilde{\mathbf{e}}^{n+1}) \nabla q_h \, ds \\ &+ (\nabla(\hat{p}^{n+1} - p^{n+1}), \nabla q_h)_\Omega + \left(\partial_t \mathbf{u}^{n+1} - \frac{\mathbf{u}^{n+1} - \mathbf{u}^n}{\delta t}, \nabla q_h \right)_\Omega \end{aligned} \tag{19}$$

Taking $q_h = \varepsilon_h^{n+1}$ yields

$$\begin{aligned} \|\nabla \varepsilon_h^{n+1}\|_{L^2(\Omega)}^2 &= -\frac{1}{\delta t} (\tilde{\mathbf{e}}_h^{n+1} - \tilde{\mathbf{e}}_h^n, \nabla \varepsilon_h^{n+1})_\Omega - \frac{1}{Re} \int_{\partial\Omega} (\mathbf{n} \times \nabla \times \tilde{\mathbf{e}}^{n+1}) \nabla \varepsilon_h^{n+1} \, ds \\ &+ (\nabla(\hat{p}^{n+1} - p^{n+1}), \nabla \varepsilon_h^{n+1})_\Omega + \left(\partial_t \mathbf{u}^{n+1} - \frac{\mathbf{u}^{n+1} - \mathbf{u}^n}{\delta t}, \nabla \varepsilon_h^{n+1} \right)_\Omega \end{aligned} \tag{20}$$

Using repeatedly the Cauchy–Schwarz inequality we obtain

$$\begin{aligned} \|\nabla \varepsilon_h^{n+1}\|_{L^2(\Omega)}^2 &\leq \frac{1}{\delta t} \|\tilde{\mathbf{e}}_h^{n+1} - \tilde{\mathbf{e}}_h^n\|_{L^2(\Omega)} \|\nabla \varepsilon_h^{n+1}\|_{L^2(\Omega)} + \frac{1}{Re} \|\nabla \times \tilde{\mathbf{e}}^{n+1}\|_{L^2(\partial\Omega)} \|\nabla \varepsilon_h^{n+1}\|_{L^2(\partial\Omega)} \\ &+ \|\nabla(\hat{p}^{n+1} - p^{n+1})\|_{L^2(\Omega)} \|\nabla \varepsilon_h^{n+1}\|_{L^2(\Omega)} \\ &+ \left\| \partial_t \mathbf{u}^{n+1} - \frac{\mathbf{u}^{n+1} - \mathbf{u}^n}{\delta t} \right\|_{L^2(\Omega)} \|\nabla \varepsilon_h^{n+1}\|_{L^2(\Omega)} \end{aligned} \tag{21}$$

This result together with (18), a standard inverse inequality, and lemma (2.3) yield

$$\|\nabla \varepsilon_h^{n+1}\|_{L^2(\Omega)}^2 \leq c((\delta t + h) + h^{-1} \|\tilde{\mathbf{e}}^{n+1}\|_{H^1(\Omega)}) \|\nabla \varepsilon_h^{n+1}\|_{L^2(\Omega)} \tag{22}$$

Hence $\|\nabla \varepsilon_h\|_{L^2(\Omega)} \leq ch^{-1}$. This result together with a standard duality argument (see Reference [21, Theorem (5.4.8)]) and Theorem 2.1 above, give the optimal estimate in the L^2 -norm

$$\|\varepsilon_h^{n+1}\|_{L^2(\Omega)} \leq c(\delta t + h) \tag{23}$$

□

Remark 2.2

It is particularly useful at low Reynolds numbers to add an additional correction to the pressure gradient as suggested by Timmermans *et al.* [22] (see also Reference [23]). Note that the pressure gradient update (6) is used only in a weak form, to substitute the pressure gradient in (4) for the next step. Then the weak form of the improved version reads

$$(\mathbf{G}_h^{n+1} - \mathbf{G}_h^n, \tilde{\mathbf{v}}_h)_\Omega = \frac{1}{\delta t} (\tilde{\mathbf{u}}_h^{n+1} - \mathbf{u}_h^{n+1}, \tilde{\mathbf{v}}_h)_\Omega + \frac{1}{Re} (\nabla \cdot \tilde{\mathbf{u}}_h^{n+1}, \nabla \cdot \tilde{\mathbf{v}}_h)_\Omega \tag{24}$$

This correction does not affect the asymptotic rate of convergence in space but improves the temporal convergence rate in the H^1 -norm if a second-order scheme is used to approximate the time derivative (see Reference [4]). This in turn improves the convergence of the pressure. It also decreases the magnitude of the L^2 error in the velocity at low Reynolds numbers, as suggested by the numerical experience of the authors. However, for the high Reynolds number numerical experiments presented below, this additional correction does not significantly change the error in the velocity and it is not used.

Remark 2.3

As already mentioned, the discretization of the advection term does not contribute to the asymptotic order of accuracy of the scheme but it can change the magnitude of the overall discretization error. Usually, the lower the divergence of the advection field, the lower the error. Since, the end-of-step velocity for the present scheme is locally divergence free, we used \mathbf{u}_h^n for the discretization of the advection in (4). The numerical results reveal that this yields a smaller overall error compared to the explicit Euler discretization using $\tilde{\mathbf{u}}_h^n$, i.e. $(\tilde{\mathbf{u}}_h^n \cdot \nabla)\tilde{\mathbf{u}}_h^n$. The numerical results with the present scheme, presented below, were produced using (4).

3. NUMERICAL RESULTS

3.1. Convergence tests

We start this section presenting the results of a convergence test using an analytic solution of the Navier–Stokes equation (with a source term) given by

$$u = \sin x \sin(y + t), \quad v = \cos x \cos(y + t), \quad p = \cos x \sin(y + t) \tag{25}$$

In the first test with analytic solutions we used a uniform structured grid produced by subdividing the domain into squares and then dividing each square into eight triangles using its diagonals and the two lines through its centroid, parallel to its sides. This grid is not exactly what is known as a cross-grid but has very similar geometrical properties to it. In Figure 1 we plot the error of the numerical solution in the $\ell^2(L^2)$ -norm versus the time step at $Re = 100$ for a variety of grids and on the time interval $[0, 5]$. The graph indicates first-order accuracy in time. The flattening observed at small time steps occurring in all the graphs presented in the figure is due to the saturation of the spatial error.

In Figure 2 we present the $\ell^2(L^2)$ - and $\ell^2(H^1)$ -errors versus the spatial step at different time steps. As anticipated, the error in the L^2 -norm is second-order accurate and that in the H^1 -norm is first-order accurate.

3.1.1. Comparisons with iso- \mathbb{P}_2 - \mathbb{P}_1 interpolation. The accuracy of the present scheme is compared to the accuracy of a first-order (in time) incremental projection scheme using iso- \mathbb{P}_2 - \mathbb{P}_1 triangular (Bercovier–Pironneau) elements on structured grids containing the same number of points and elements as for the present scheme. The overall structure of the grid is slightly different because of the specific requirements of the Bercovier–Pironneau elements. In both cases, however, the interpolation error for the velocity is $O(h^2)$ in the L^2 -norm. The results for the analytic solution (25) and $Re = 100$ are presented in Table I. The errors in the

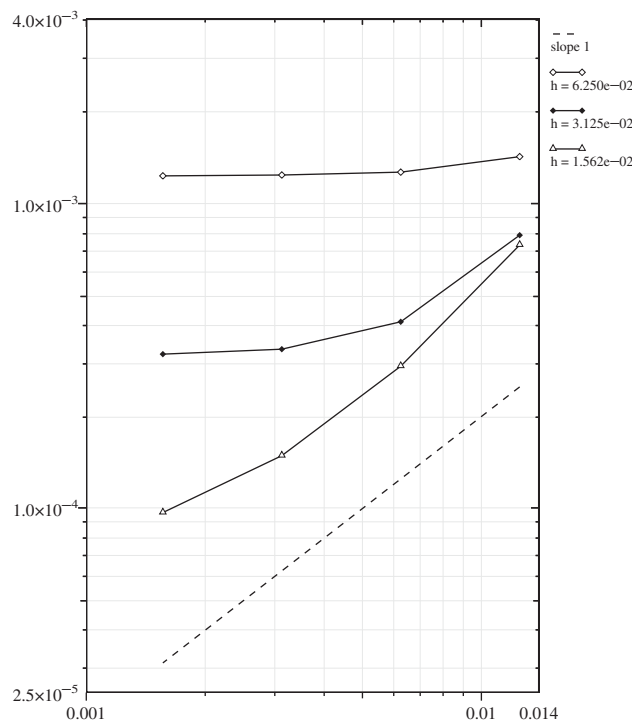


Figure 1. Error in velocity in $\ell^2(L^2)$ -norm versus the time step δt , $T = 5$, $Re = 100$, for a variety of grid sizes.

table are for the predicted velocity $\tilde{\mathbf{u}}^{n+1}$ in both cases. The present projection is comparable in accuracy with the projection using iso- \mathbb{P}_2 - \mathbb{P}_1 elements. It is also comparable in accuracy to the classical projection using the Crouzeix–Raviart element for both, the momentum equation and for the projection step. Figure 3 shows the $l^2(0, 5; L^2([0, 1] \times [0, 1]))$ error for the problem with the analytic solution given above, using the present scheme and an incremental projection with the Crouzeix–Raviart spatial approximation. The two approximations are compared on the generalized Stokes problem (with the advection terms excluded) because the advection with the generally discontinuous Crouzeix–Raviart approximation for the velocity should be treated in the spirit of the discontinuous Galerkin methods and will depend on the setting for the interfacial fluxes. This is beyond the scope of the present study and we skipped the advection terms for the sake of a fair comparison. The two schemes clearly yield very similar results. They both exhibit superconvergence in time which should be due to the specific solution of the problem. In Figure 4 we present the results for the convergence in time but using a second-order backward difference scheme in time. The convergence for the velocity is expected to be second-order in both L^2 and H^1 norm and this is clearly demonstrated by the numerical results.

3.1.2. Diagonal grids. As we pointed out in Section 2.1 the existence of a divergence free \mathbb{P}_1 interpolant on general grids is not guaranteed and without it we have been able to establish

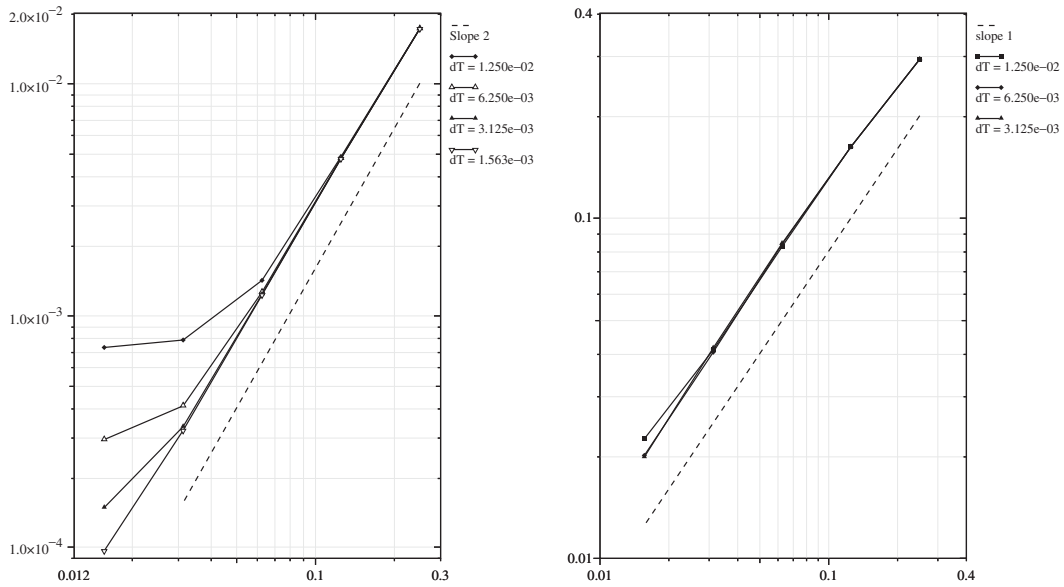


Figure 2. Error in velocity in $\ell^2(L^2)$ and $\ell^2(H^1)$ -norm versus the grid size h , $T = 5$, $Re = 100$, for a variety of time steps.

Table I. Comparison of the $\ell^2(0, 5; L_2(\Omega))$ and $\ell^2(0, 5; H^1(\Omega))$ -norms of the velocity error for different time steps, δt , and different meshsize h ; Reynolds number $Re = 100$.

| δt | h | $\ell^2(0, 5; L_2(\Omega))$ -norm | | $\ell^2(0, 5; H^1(\Omega))$ -norm | |
|------------|------|--------------------------------------|----------------|--------------------------------------|----------------|
| | | iso- \mathbb{P}_2 - \mathbb{P}_1 | Present scheme | iso- \mathbb{P}_2 - \mathbb{P}_1 | Present scheme |
| 0.0500000 | 1/8 | 1.702290e-02 | 1.0051450E-02 | 3.850517e-01 | 1.8557660E-01 |
| 0.0250000 | 1/8 | 1.623382e-02 | 5.3463740E-03 | 3.818002e-01 | 1.6369440E-01 |
| 0.0125000 | 1/8 | 1.617754e-02 | 4.8185810E-03 | 3.815409e-01 | 1.6200860E-01 |
| 0.0062500 | 1/8 | 1.618194e-02 | 4.7534930E-03 | 3.816086e-01 | 1.6191400E-01 |
| 0.0031250 | 1/8 | 1.618895e-02 | 4.7361680E-03 | 3.816846e-01 | 1.6186320E-01 |
| 0.0015625 | 1/8 | 1.619345e-02 | 4.7284610E-03 | 3.817329e-01 | 1.6181490E-01 |
| 0.0500000 | 1/16 | 5.855242e-03 | 8.8821840E-03 | 1.540878e-01 | 1.2183130E-01 |
| 0.0250000 | 1/16 | 3.367833e-03 | 2.6469600E-03 | 1.435928e-01 | 8.5758860E-02 |
| 0.0125000 | 1/16 | 3.046877e-03 | 1.4165660E-03 | 1.423505e-01 | 8.2413190E-02 |
| 0.0062500 | 1/16 | 3.003900e-03 | 1.2606420E-03 | 1.421816e-01 | 8.3748370E-02 |
| 0.0031250 | 1/16 | 2.998113e-03 | 1.2336630E-03 | 1.421746e-01 | 8.4228420E-02 |
| 0.0015625 | 1/16 | 2.998189e-03 | 1.2257410E-03 | 1.421884e-01 | 8.4313620E-02 |
| 0.0500000 | 1/32 | 4.905032e-03 | 8.8466680E-03 | 8.323091e-02 | 1.0610640E-01 |
| 0.0250000 | 1/32 | 1.579660e-03 | 2.3649390E-03 | 5.455816e-02 | 5.0030510E-02 |
| 0.0125000 | 1/32 | 7.565248e-04 | 7.8401870E-04 | 5.085209e-02 | 4.0976360E-02 |
| 0.0062500 | 1/32 | 5.509742e-04 | 4.0827610E-04 | 5.028274e-02 | 4.0347290E-02 |
| 0.0031250 | 1/32 | 4.993708e-04 | 3.3217460E-04 | 5.016987e-02 | 4.1510130E-02 |
| 0.0015625 | 1/32 | 4.863987e-04 | 3.1999660E-04 | 5.014688e-02 | 4.2656160E-02 |

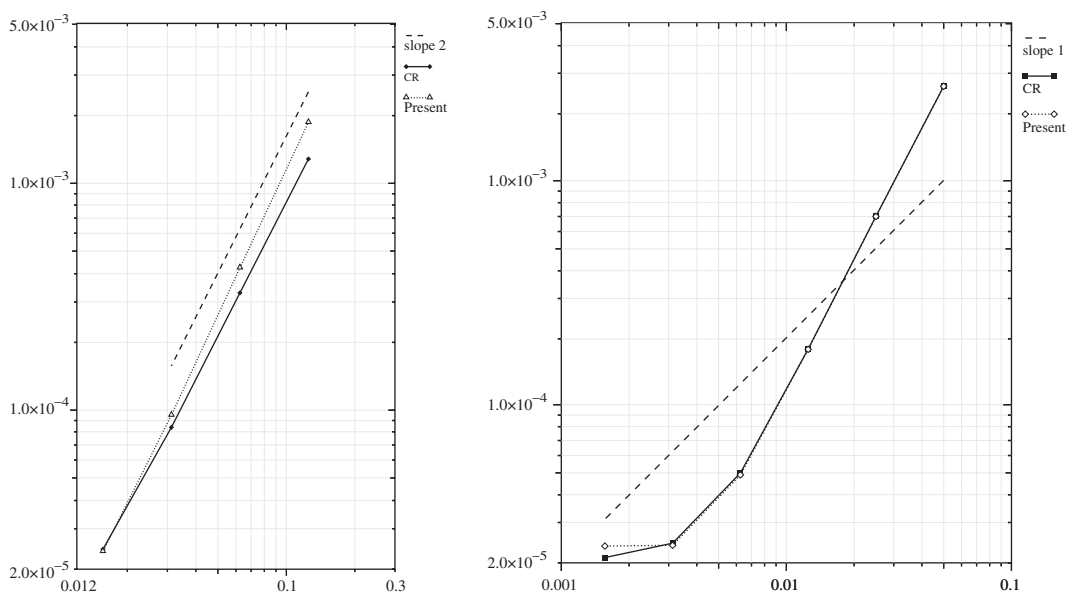


Figure 3. Error in velocity in $\ell^2(L^2)$ -norm versus the grid size h , $\delta t = 0.003125$ (left graph), and versus the time step δt , $h = 1/64$ (right graph); $T = 5$, $Re = 0$. The results are produced with an incremental scheme using Crouzeix–Raviart elements for both, the momentum equation and the projection (CR) and using the present scheme (present).

only suboptimal convergence estimate on the velocity. The numerical results on diagonal grids presented below show that the convergence rate of the velocity is close to optimal although the only divergence free \mathbb{P}_1 interpolant on such grids is the zero field (velocity locking).

A close inspection of the locking phenomenon reveals that it can occur on two-dimensional grids for which there is at least one internal node that is connected to more than two boundary nodes via elemental edges. We will demonstrate this using a diagonal grid on a square domain. In Figure 5 we show the upper left corner of such a grid. Since the velocity is prescribed at the boundary, the incompressibility condition in two of the elements t_2, t_3 , or t_4 uniquely determines the value of the velocity at n_1 (the flux through the edge e_1 is fixed by the boundary conditions). Therefore, it is impossible to satisfy the incompressibility condition in the third element unless the velocity at n_1 is equal to zero (we presume zero Dirichlet boundary conditions for the velocity). This argument applies to the neighbours of n_1 and so on; as a result, the only divergence-free \mathbb{P}_1 interpolant is equal to zero. However, if the incompressibility is not imposed in the elements t_1, t_2, t_3, t_4 and the similar cluster of elements in the lower right corner of the grid, a divergence free interpolant can be constructed in the rest of the domain. In the context of the present scheme the local incompressibility of $\tilde{\mathbf{u}}_h^{n+1}$ is not enforced and therefore it can be compromised in the cluster t_1, t_2, t_3, t_4 . Since the number of such elements is independent of the grid parameter h , it seems that this does not spoil the convergence of the scheme.

Another way of observing that locking can be avoided consists of considering a Stokes problem with a steady solution. Let us denote by \mathbf{u}_h and $\tilde{\mathbf{u}}_h$ the limit of \mathbf{u}_h^{n+1} and $\tilde{\mathbf{u}}_h^{n+1}$ as n

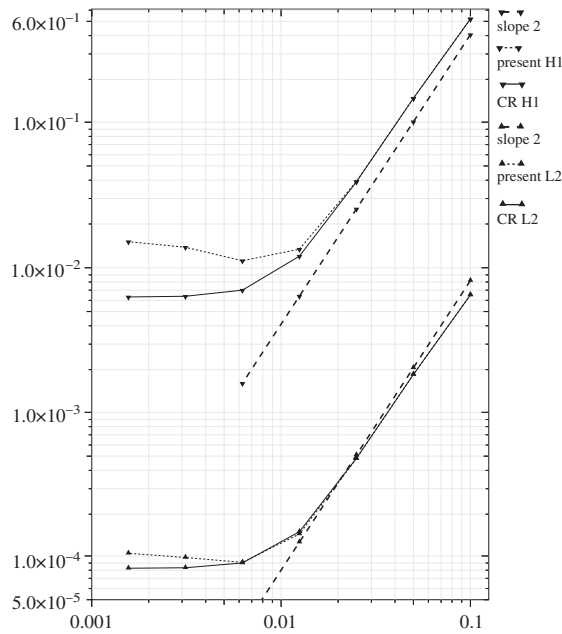


Figure 4. Error in velocity in $\ell^2(L^2)$ and $\ell^2(H^1)$ norms versus the time step δt , $h = 1/32$; $T = 5$, $Re = 0$. The results are produced with a second-order-in-time incremental scheme using Crouzeix–Raviart elements for both, the momentum equation and the projection (CR) and using the present scheme (present).

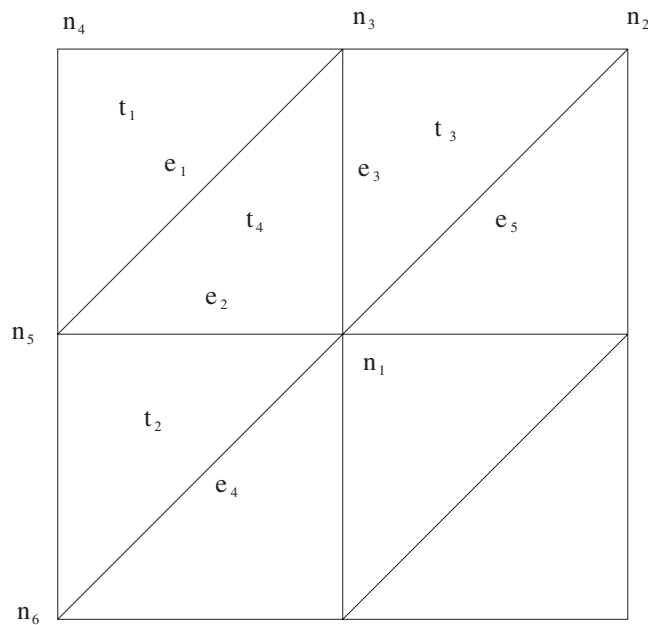


Figure 5. Diagonal grid.

Table II. The $\ell^2(0, 5; L_2(\Omega))$ -norm of the velocity error using a diagonal grid, different time steps, δt , and a different meshsize h ; Reynolds number $Re = 100$.

| $\delta t/h$ | 1/8 | 1/16 | 1/32 | 1/64 | 1/128 |
|--------------|--------------|--------------|--------------|--------------|--------------|
| 0.0500000 | 1.07102e-02 | 1.002422e-02 | 1.015209e-02 | 1.027519e-02 | 1.033813e-02 |
| 0.0250000 | 5.23603e-03 | 2.801070e-03 | 2.643430e-03 | 2.652358e-03 | 2.665173e-03 |
| 0.0125000 | 4.61674e-03 | 1.296322e-03 | 8.219813e-04 | 7.832054e-04 | 7.826101e-04 |
| 0.0062500 | 4.47716e-03 | 1.177908e-03 | 3.887040e-04 | 2.988708e-04 | 2.903357e-04 |
| 0.0031250 | 4.33028e-03 | 1.416590e-03 | 3.177499e-04 | 1.498433e-04 | 1.324947e-04 |
| 0.0015625 | 3.681704e-03 | 1.641200e-03 | 5.048719e-04 | 1.043321e-04 | 6.791169e-05 |

goes to infinity, respectively. Since there are spurious pressure modes, there is \mathbf{G}_h (a spurious gradient) such that $\mathbf{u}_h - \tilde{\mathbf{u}}_h = \mathbf{G}_h \in \mathbf{Y}_h$ and $(\mathbf{G}_h, \mathbf{v}) = 0$ for all $\mathbf{v} \in \mathbf{X}_h$. Since there is nothing in the projection algorithm which enforces \mathbf{G}_h to be zero (which would not have been the case, had the inf-sup condition been satisfied), enforcing \mathbf{u}_h to be locally solenoidal does not automatically enforce $\tilde{\mathbf{u}}_h$ to be so; hence locking is avoided.

The performance of the method on diagonal grids is demonstrated using the solution given by (25). The results are shown in Table II. The scheme clearly has an optimal convergence rate on such grids. It was noticed, however, that on certain problems leading to a steady solution, the convergence of the approximate solution to the steady state was influenced by the grid type. The convergence on cross-grids was much faster than the convergence on diagonal grids.

3.2. Pressure recovery

Finally, we verify the convergence properties of the pressure which is recovered by means of (14). We made three series of computations using cross grids. In the first one we computed the Lagrange multiplier derived from the projection step of the present scheme (see (7)). In the second test we use the Crouzeix–Raviart element in both the momentum equation and the projection step. In the third test we used the scheme proposed in the paper and we recovered the pressure by using (14). In Figure 6 we present for the above three techniques the error on the pressure in the $\ell^2(L^2)$ -norm as a function of the mesh size (left panel) and as a function of the time step (right panel). In the three cases we used a first-order-in-time incremental scheme. The Lagrange multiplier associated with (7) diverges at small time steps, whereas the Lagrange multiplier associated with the Crouzeix–Raviart approximation converges. The pressure recovered by using (14) converges nicely. In the last two cases the convergence rate is slightly better than first-order, i.e. the pressure approximation is superconvergent for this particular solution.

3.3. Lid-driven cavity

Beside the convergence tests presented above we validated the present scheme on two problems which are well documented in the literature. The first validation problem is the lid-driven cavity flow in two dimensions. The results from the present scheme are compared with the very accurate numerical results from Reference [24]. In Reference [24] the authors employed

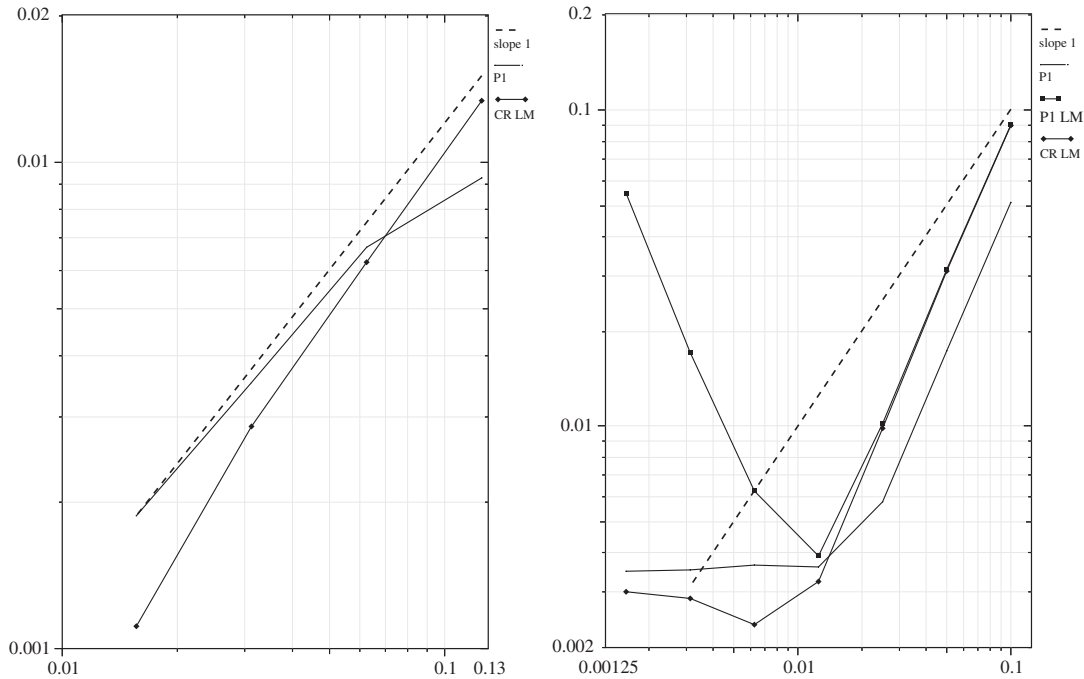


Figure 6. Error on the pressure in $\ell^2(L^2)$ -norm versus the grid size h , $\delta t = 0.003125$ (left panel) and versus the time step δt , $h = 1/32$ (right panel); $T = 5$, $Re = 0$. The results are produced with the incremental scheme using Crouzeix–Raviart elements for the momentum equation and the projection, and using the present scheme with pressure recovery. P1 LM: Lagrange multiplier of the projection step of the present scheme; CR LM: Lagrange multiplier of the projection step with Crouzeix–Raviart elements; P1: pressure recovered by means of (14).

a vorticity-streamfunction finite difference scheme with a multigrid relaxation and solved directly the steady equations on a 128×128 grid. We computed the steady solution on a grid of 32×32 points using the present scheme and the iso- \mathbb{P}_2 - \mathbb{P}_1 incremental projection. The results at different Reynolds numbers are compared in Figure 7. Obviously, the two sets of data practically match each other. The differences are smaller than 10^{-4} in the L^∞ -norm.

3.4. Square cylinder

The last validation problem is the vortex shedding around a square cylinder. This problem is essentially unsteady and is a well documented reference test case [25]. The Reynolds number is $Re = 100$ and the angle of incidence made by the flow at infinity is zero (two sides of the square being horizontal). The dimensions of the flow domain are $16d \times 25d$ where d is the length of one side of the square cylinder. The cylinder is placed at a distance of $8d$ from the inlet and $16d$ from the outlet. The spatial step size is $h = 0.25$ away from the cylinder and $h = 0.1$ in its vicinity and in its wake. The evolution of the vertical velocity component at a point which is at a distance d downstream from the cylinder and at the horizontal centreline of the domain is presented in Figure 8. The Strouhal number of the vortex shedding reported

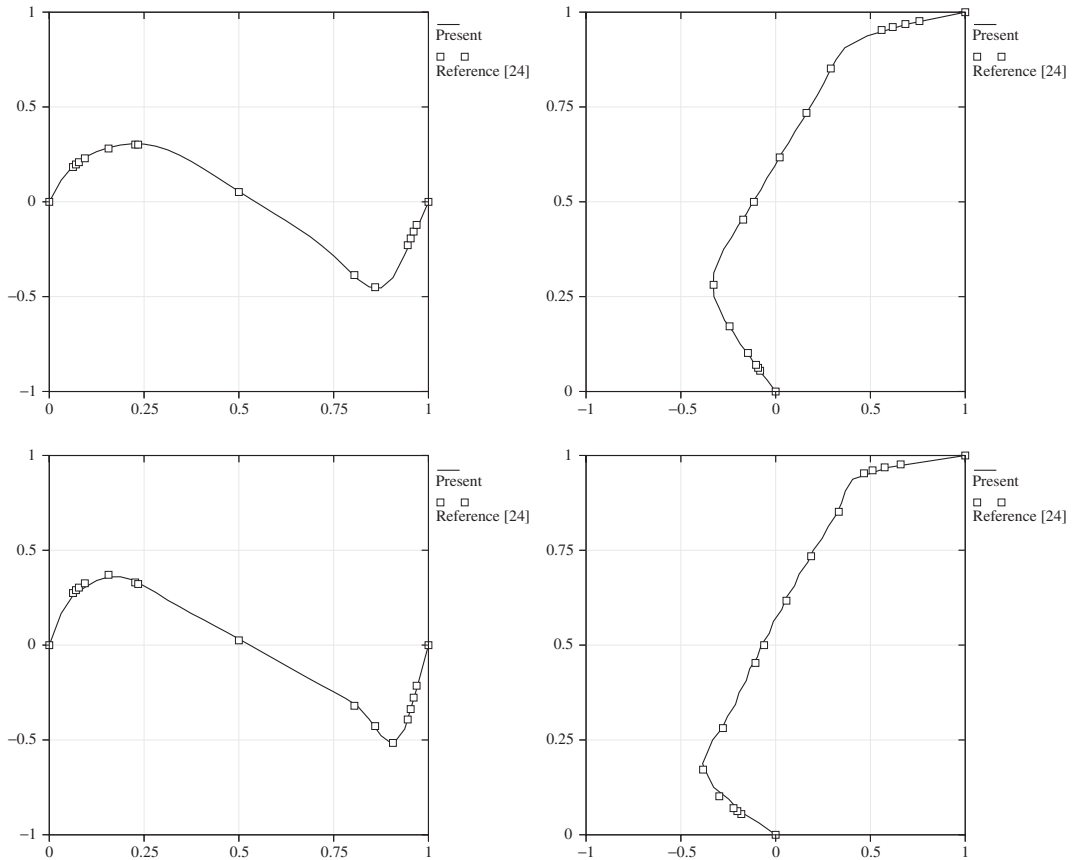


Figure 7. Lid-driven cavity flow at $Re = 400$ (Top) and $Re = 1000$ (Bottom). Horizontal (left column) and vertical (right column) velocity profiles through the centre of the cavity.

in Reference [25] varies between 0.133 and 0.15 depending on the outlet boundary conditions and the dimensions of the computational domain. The Strouhal number obtained by the present simulation using a first-order time marching is equal to 0.133.

4. CONCLUSIONS

We proposed a projection scheme for the Navier–Stokes equations which uses a conforming \mathbb{P}_1 interpolation for the velocity in the momentum equation and a non-conforming \mathbb{P}_1 interpolation for the velocity at the projection step. An advantage of this scheme is that the end-of-step velocity is pointwise divergence free over each element and therefore it is recommendable for problems requiring good mass conservation, for example free-boundary problems. The projection step can be performed either using the explicit basis of the divergence-free subspace of the non-conforming \mathbb{P}_1 space or using the traditional Lagrange multiplier approach. In the

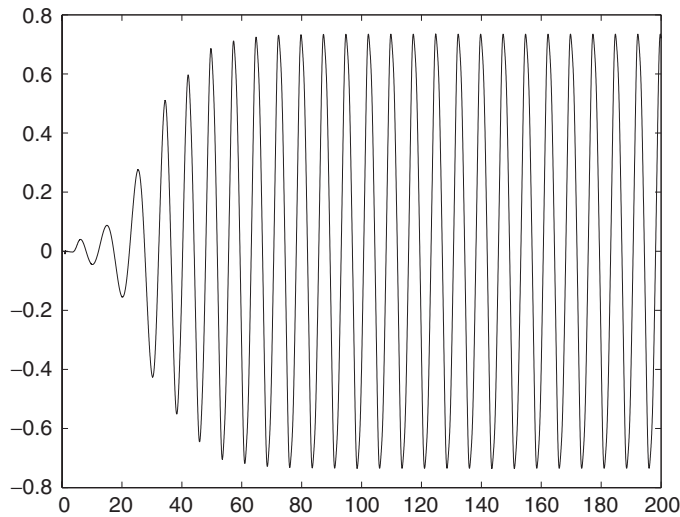


Figure 8. Time history at a point behind the cylinder, $Re = 100$.

first case the resulting linear system at the projection step is about two times smaller (in two dimensions) than that in the second case. A disadvantage of the scheme is that the pressure is either not computed explicitly (in the first case) or contains spurious modes and requires additional filtering. In this paper we suggest and analyse one possible algorithm for a pressure recovery. Although it requires the solution of a scalar Poisson problem, it is not necessary to recover the pressure on each time step and therefore it does not increase significantly the cost of the computation.

ACKNOWLEDGEMENTS

The first and third authors would like to acknowledge the support, under a Discovery Grant, of the National Science and Engineering Research Council of Canada (NSERC).

REFERENCES

1. Girault V, Raviart P-A. *Finite Element Methods for Navier–Stokes Equations*. Springer Series in Computational Mathematics (Theory and Algorithms). Springer: Berlin, 1986.
2. Temam R. Sur l’approximation de la solution des équations de Navier–Stokes par la méthode des pas fractionnaires ii. *Archive for Rational Mechanics and Analysis* 1969; **33**:377–385.
3. Chorin AJ. Numerical solution of the Navier–Stokes equations. *Mathematics of Computation* 1968; **22**:745–762.
4. Guermond J-L, Shen J. On the error estimates for the rotational pressure-correction projection methods. *Mathematics of Computation* 2001; **333**:1111–1116.
5. Guermond J-L, Shen J. Velocity-correction projection methods for incompressible flows. *SIAM Journal on Numerical Analysis* 2003; **41**:112–134.
6. Guermond J-L, Mineev P, Shen J. Numerical issues on projection methods. *Computer Methods in Applied Mechanics and Engineering*, in press.
7. Quarteroni A, Saleri F, Veneziani A. Factorization methods for the numerical approximation of Navier–Stokes equations. *Computer Methods in Applied Mechanics and Engineering* 2000; **188**(1–3):505–526.
8. Guermond J-L. Some practical implementations of projection methods for Navier–Stokes equations. *Modélisation Mathématique et Analyse Numérique* 1996; **30**:637–667. Also in *Comptes Rendus de l’Académie des Sciences Paris, Série I* 1994; **319**:887–892.

9. Guermond J-L, Quartapelle L. Calculation of incompressible viscous flows by an unconditionally stable projection FEM. *Journal of Computational Physics* 1997; **132**:12–23.
10. Gresho P, Sani RL. *Incompressible Flow and the Finite Element Method*. Wiley: New York, 1998.
11. Turek S. A comparative study of time-stepping techniques for the incompressible Navier–Stokes equations: from fully implicit nonlinear schemes to semi-implicit projection methods. *International Journal for Numerical Methods in Fluids* 1996; **22**:987–1011.
12. Crouzeix M, Raviart P-A. Conforming and non-conforming finite element methods for solving the stationary Stokes equations. *RAIRO—Analyse Numérique* 1973; **3**:33–75.
13. Cockburn B, Kanschat G, Schotzau D, Schwab C. Local discontinuous Galerkin methods for the Stokes system. *SIAM Journal on Numerical Analysis* 2002; **40**(1):319–343.
14. Brezzi F, Fortin M. *Mixed and Hybrid Finite Element Methods*. Springer: New York, 1991.
15. Guermond J-L, Quartapelle L. On the approximation of the unsteady Navier–Stokes equations by finite element projection methods. *Numerische Mathematik* 1998; **80**(5):207–238.
16. Guermond J-L. Un résultat de convergence d'ordre deux en temps pour l'approximation des équations de Navier–Stokes par une technique de projection incrémentale. *M2AN Mathematical Modelling and Numerical Analysis* 1999; **33**(1):169–189. Also in *Comptes Rendus de l'Académie des Sciences Paris, Série I* 1997; **325**: 1329–1332.
17. Cuvelier C, Segal A, van Steenhoven AA. *Finite Element Methods and the Navier–Stokes Equations*. D. Reidel: Dordrecht, 1986.
18. Hecht F. Construction d'une base de fonctions p_1 non conforme à divergence nulle dans ir^3 . *RAIRO—Analyse Numérique* 1981; **15**:119–150.
19. Dörfler W. The conditioning of the stiffness matrix for certain elements approximating the incompressibility condition in fluid dynamics. *Numerische Mathematik* 1990; **13**:203–214.
20. Qin J. On the convergence of some low order mixed finite element methods for incompressible fluids. *Ph.D. Thesis*, The Pennsylvania State University, 1994.
21. Brenner SC, Scott LR. *The Mathematical Theory of Finite Element Methods, Texts in Applied Mathematics*, vol. 15. Springer: New York, 1994.
22. Timmermans LJP, Minev PD, Van De Vosse FN. An approximate projection scheme for incompressible flow using spectral elements. *International Journal for Numerical Methods in Fluids* 1996; **22**:673–688.
23. Minev P, Gresho PM. A remark on pressure correction schemes for transient viscous incompressible flow. *Communications in Numerical Methods in Engineering* 1998; **14**:335–346.
24. Ghia U, Ghia KN, Shin CT. High-resolutions for incompressible flow using the Navier–Stokes equations and a multigrid method. *Journal of Computational Physics* 1982; **48**(1):387–411.
25. Sohankar A, Norberg C, Davidson L. Low-Reynolds-number flow around a square cylinder at incidence: study of blockage, onset of vortex shedding and outlet boundary condition. *International Journal for Numerical Methods in Fluids* 1998; **26**:39–56.